Journal of Applied Electrochemistry 34: 1241–1248, 2004.

Flow influenced electrochemical corrosion of nickel aluminium bronze – Part II. Anodic polarisation and derivation of the mixed potential

G. KEAR[1]*, B.D. BARKER[2], K. STOKES[3] and F.C. WALSH[4]
[1]*Building Research Association of New Zealand (BRANZ) Ltd., Private Bag 50 908, Porirua City 6220, New Zealand*
[2]*Applied Electrochemistry Group, Centre for Chemistry, University of Portsmouth, PO1 2DT, UK*
[3]*DSTL Winfrith, Winfrith Technology Park, Dorchester DT2 8WX, UK*
[4]*Electrochemical Engineering Group, School of Engineering Sciences, University of Southampton, Highfield SO17 1BJ, UK*
*(*author for correspondence, e-mail: garethkear@branz.co.nz)*

Received 12 November 2003; accepted in revised form 13 July 2004

Key words: flow-enhanced corrosion, mass transfer, nickel aluminium bronze, rotating cylinder electrode, rotating disc electrode, seawater

Abstract

The mixed charge and mass transfer influenced anodic current response of CA 104 nickel aluminium bronze (NAB) is presented as a function of both laminar (rotating disc electrode) and fully turbulent (rotating cylinder electrode) fluid flow. At low values of positive polarisation, the overall behaviour of the freshly polished material in filtered and artificial seawaters is closely related to that of unalloyed copper. The primary anodic reaction in this case is the selective dissolution of the copper component via a cuprous di-chloride complex anion. At large positive polarisation, the solid solution mole fraction for the production of a discrete film of protective alumina (Al_2O_3) is examined as a function of Reynolds number and discussed in terms of a new mechanism for the passivation NAB in seawater. The polarisation data is used to replicate experimental Reynolds number dependent, corrosion potentials and corrosion current densities over a wide range of electrode angular velocities.

1. Introduction

The addition of aluminium increases the corrosion resistance of copper in seawater, sulphuric acid and general salt solutions. The alloying element also provides good wear properties and resistance to high temperature oxidation [1]. The corrosion resistance of both aluminium bronze and nickel aluminium bronze (NAB) alloys has been attributed to a sustainable protective layer of alumina, which builds up quickly on the alloy surface post-exposure to the corrosive environment [2, 3]. Additions of nickel and iron enable greater amounts of aluminium to be present in the alloy (9–11%) before chemically and mechanically detrimental Cu_9Al_4 phases are produced [1, 4].

The majority of literature on NAB corrosion has centred upon marine cavitation damage [5] exposure tests [6–8] and case histories [9]. From this work, it is clear that the dissolution rate of the alloy can exhibit the flow rate dependence commonly observed with other copper-based alloys [10, 11]. General weight loss derived, dissolution rates in NAB seawater pipe flow can range from 0.05 mm y^{-1} (2 μA cm^{-2}) under static conditions up to 1 mm y^{-1} (36 μA cm^{-2}) within turbulent and impinging fluid regimes.

NAB linear polarisation resistance (LPR) measurements made by Schussler and Exner in artificial seawater [2, 3] were relatively high (5–10 μA cm^{-2}) although dissolution rates decreased with time of exposure to reach around 0.5 μA cm^{-2}. A mean anodic Tafel slope of 0.064 V $decade^{-1}$ was calculated for freshly polished surfaces and the number of electrons exchanged in the rate-determining steps of both reactions was determined as 1. Schussler and Exner also proposed that after a potential (E) step to −0.190 V vs saturated calomel electrode (SCE), corresponding to a polarisation of approximately +50 to 100 mV, an alumina-based, protective film formed. Film formation corresponded with a notable decrease in the apparent flow dependence of the current response.

In Part I of this series of papers, the cathodic characteristics of NAB were discussed [12]. In this work, the electrochemical characteristics of the anodic dissolution of NAB are examined using the rotating disc electrode (RDE) and the rotating cylinder electrode (RCE) and used in the derivation of the corrosion potential (E_{corr}) or mixed potential. The hitherto unexamined dependency of the overall corrosion rate on fluid flow conditions will also be determined using the high reproducible laminar and turbulent fluid flow regimes resent at the RDE and

RCE geometries. The influence of Reynolds number (*Re*) on the mass transfer coefficient (k_m) as a function of laminar flow (RDE) and fully turbulent flow (RCE) for hydrodynamically smooth surfaces has been fully described in the literature (see Part I).

2. Experimental procedure

Wrought NAB material was supplied by Stone Manganese Ltd. (UK) in rod form to meet BS 2874: 1986: CA 104. The composition of the alloy is given in Table 1. The design and construction of RDE (area 0.126 cm^2) and RCE (area 10.06 cm^2) is described in Part I [12]. Working electrode surfaces were mechanically polished (manually) on micro-polishing cloth and degreased in ethanol prior to each individual polarisation and corrosion potential measurement. Mechanical polishing of pre-conditioned electrodes consisted of a double, 3-min polish with a 0.3 μm α-alumina/distilled water slurry.

Two electrolytes were used: filtered and conductivity adjusted seawater (originally taken from Langstone Harbour, Hampshire, UK) and an artificial seawater (to BS 3900:Part F4:1968, supplied by BDH). A comprehensive review of the electrolyte pre-treatment process and its subsequent characterisation is given in Part I.

All electrochemical measurements were made at 25 ± 0.2 °C with an Eco Chemie Autolab potentiostat (PGSTAT20 computer controlled) using the General Purpose, Electrochemical Software (GPES) version 4.5. The electrochemical cell incorporated a thermostatically controlled, glass water jacket, a platinum gauze counter electrode and a Radiometer Analytical A/S, REF 401, SCE used in conjunction with either a RDE or RCE adapted Luggin–Haber capillary. The range of Reynolds numbers (*Re*) for each geometry was $Re_{\mathrm{RDE}} = 79$–3700 (corresponding to 200–9500 rpm or 29–995 rad s^{-1}) and $Re_{\mathrm{RCE}}=1900$–76,860 (100–4000 rpm or 10–419 rad s^{-1}). Anodic linear sweep voltammetry (LSV) was performed at the relatively high potential sweep rate of 1 mV s^{-1} in order to minimise surface disruption during measurements.

Table 1. Alloy percentage elemental composition (wt./wt.) conforming to BS 2874: 1986: CA 104 (suppliers analysis)

Cu	Fe	Si	Mn	Pb	Al	Ni	Mg	Zn
Bal.	4.43	0.05	0.14	0.02	9.31	4.65	0.01 max.	0.11

3. Results and discussion

3.1. *Corrosion potential*

After initial immersion at a given angular velocity, the directly measured mixed potential or corrosion potential of the NAB became more negative until a stabilised potential was achieved (Figure 1). This behaviour has also been previously observed for unalloyed copper at both the RDE [13] and RCE [14]. The period of time required to achieve equilibration decreased with increasing angular velocity. For Re_{RDE} values of 79 and 3700, approximate times for stabilisation were 800 and 300 s, respectively. This observation has been associated with the diffusion-controlled chloride ion facilitated dissolution of a relatively noble cuprous oxide-based film formed during the mechanical polishing of copper-based materials [15]. For example:

$$Cu_2O + H_2O + 4Cl^- \Leftrightarrow 2CuCl_2^- + 2OH^- \qquad (1)$$

Moreover, the observed increase in negative shift of the corrosion potential at increasing *Re* (from approximately −0.295 to −0.335 V for Re_{RDE} 79 and 3700) indicates that the corrosion mechanism of freshly polished NAB has a definite flow rate dependency [16]. This latter point will be discussed in more detail in the derivation of the mixed potential (Section 3.3).

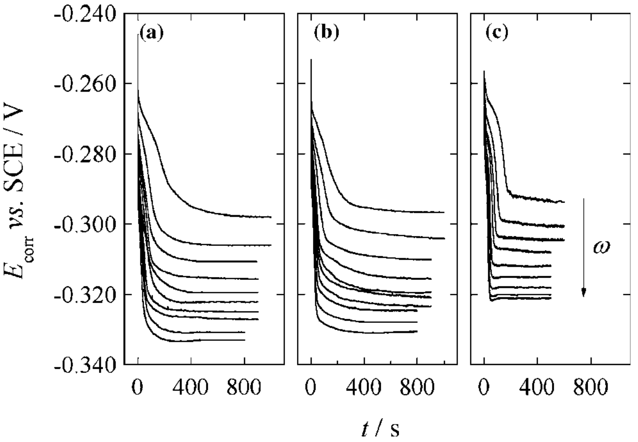

Fig. 1. Mean corrosion potential transients for NAB as a function of electrode angular velocity. Re_{RDE}=79–3700 (21, 42, 84, 126, 188, 251, 378, 503, 681 and 995 rad s^{-1}); Re_{RCE}=1900–26,900 (10, 21, 42, 84, 126, 189, 251, 367 and 419 rad s^{-1}).

3.2. *Anodic dissolution*

Anodic LSV was used as a function of RDE rotation rate in order to determine the large positive polarisation characteristics of the material (Figure 2). The voltammetry showed a definite rotation rate dependence on both the passivation peak current density and the 'passive' limiting current density. Between 21 and 84 rad s^{-1} (Re_{RDE} = 79 and 316), the typical quasi-passivation behaviour, frequently observed in the literature for copper and copper nickels [15, 17–20], dominated. At these velocities, the polarisation response for these materials has three main potential regions of interest:

1. an exponential region of apparent mixed charge transfer and mass transport controlled current (up to a polarisation of approximately +0.1 V),
2. a region of film formation (resulting in a current peak) followed by a mass transfer dependent limit-

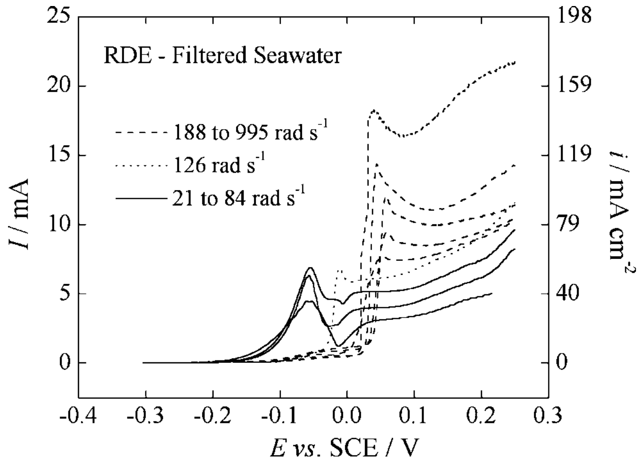

Fig. 2. Anodic LSV as a function of RDE angular velocity at 21, 42, 84, 126, 188, 251, 378, 503, 681 and 995 rad s^{-1} (Re_{RDE}=79–3700). (a) RDE – artificial seawater, (b) RDE – filtered seawater and (c) RCE – filtered seawater.

ing current density (approximately +0.2 to +0.5 V), and

3. a region of increased current density due to the formation of Cu(II) species (polarisation, approximately > +0.5 V).

At 188 rad s^{-1} (1800 rpm or Re_{RDE}=700) and above, however, an apparent self-passivating mechanism was observed where the rate of reaction was effectively inhibited (no passivation peak) until a relatively positive critical applied potential was achieved ($E_{\mathrm{crit}} \cong +0.025$ V vs SCE). Above E_{crit}, the current density stepped directly to a convective-diffusion controlled value of limiting current density (j_{L}).

It is possible to explain this change in mechanism by considering the limiting mole fraction for aluminium oxide formation ($N_{\mathrm{Al_2O_3}}$). For Cu–Al alloys, passivation is based on aluminium having a greater affinity for O_2 than copper [21]. From enthalpies of formation, Al_2O_3 (1578 kJ mol^{-1} of oxide) is considerably more stable than a probable alternative, Cu_2O (145 kJ mol^{-1}). For aluminium, bronzes it has been shown that a rapid dissolution of copper will lead to the achievement of $N_{\mathrm{Al_2O_3}}$. Protection is then afforded as Al_2O_3 is an insulator and highly impermeable to the passage of cuprous cations which can no longer enter what is the outermost layer of cuprous oxide [21].

Here, the limiting mole fractions for Al_2O_3 and NiO formation at NAB were calculated [15] as approximately 0.65 (Al) and 0.51 (Ni), respectively. It is probable that, during anodic polarisation, the limiting mole fraction for the formation of pure Al_2O_3 was achieved at rotation rates above 1800 rpm due to the greater mass transfer enhanced, non-electrochemical dissolution of the copper or the copper-based corrosion products via $CuCl_2^-$ formation. At lower angular velocities, the dissolution rate of the Cu-based material is low in comparison to its rate of formation. Under these conditions the electrodissolution of the alloy will be restricted either by a pure film of Cu_2O or, more probably, a mixed oxide of Cu_2O/Al_2O_3. These semiconducting oxide films will have low resistivity relative to pure Al_2O_3 [22], thus enabling sustained dissolution at greater rates. It appears, therefore, that the rapid rate of initial corrosion produced by high rates of mass transfer can initiate very effective alloy passivation.

At potentials more positive than E_{crit}, however, the Al_2O_3 passive film breaks down and the alloy dissolves under full mass transfer control as at the low angular velocities.

The influence of film growth on mass transfer controlled currents at low positive polarisation was minimised experimentally using a potential step current transient (PSCT) technique with controlled hydrodynamic steps and a limited experimental time scale (Figure 3). Excellent reproducibility (maximum deviation ±0.03 mA cm^{-2} over a minimum of three trials throughout) enabled an examination of the anodic response close to the corrosion potential at very small increments of polarisation (typically 5 mV).

The anodic dissolution of copper is usually considered to be a reversible process which is under mixed charge and mass transfer control at very low anodic polarisation [17, 18, 20, 23–32]. Generally, the literature describes apparent 'Tafel' slopes of approximately 0.060 V decade^{-1} within the mixed controlled region. This relationship has been described for a hydrodynamically smooth RDE through Equation 2 [26],

$$\frac{\mathrm{d}\log\left(\mathrm{d}j^{-1}/\mathrm{d}\omega^{-0.5}\right)}{\mathrm{d}E} = \frac{-zF}{2.3RT} \tag{2}$$

where, E, ω, z and F are the electrode potential, angular velocity, stoichiometric number of electrons exchanged and the Faraday constant, respectively. R and T are the molar gas constant and the absolute temperature.

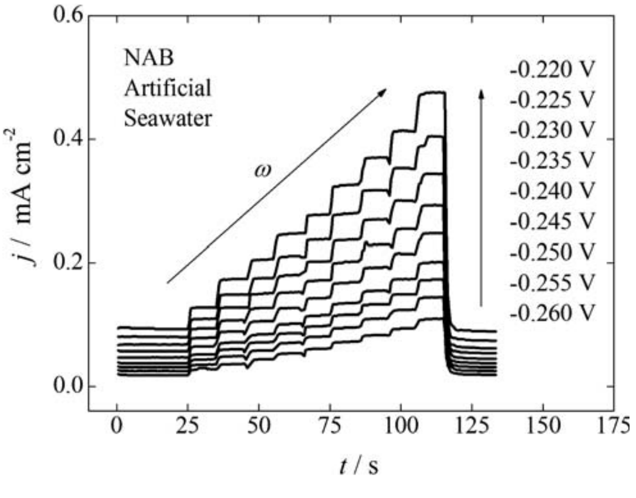

Fig. 3. Mixed charge and mass transfer controlled electrodissolution of the NAB RDE measured as a function of applied potential using a potential step, current transient technique with hydrodynamic (angular velocity) steps of 21, 42, 84, 126, 188, 251, 378, 503, 681, 995 and 21 rad s^{-1} (Re_{RDE}=79–3700).

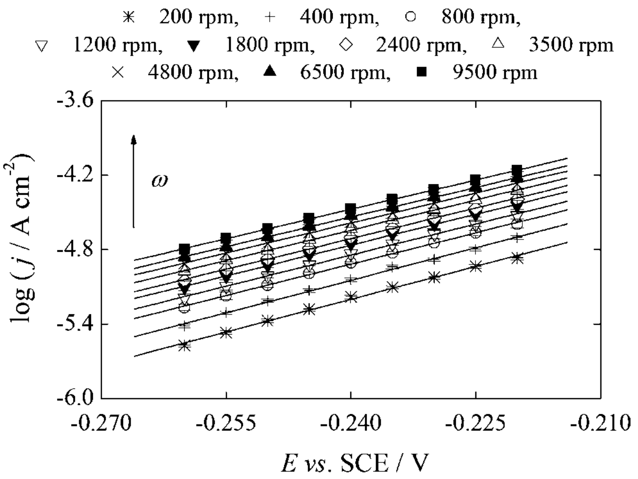

Fig. 4. Apparent 'Tafel' slopes (corrected for oxygen reduction) describing the anodic dissolution of NAB as a function RDE of angular velocities of 21, 42, 84, 126, 188, 251, 378, 503, 681 and 995 rad s^{-1} (Re_{RDE}=79–3700).

Figure 4 describes such apparent Tafel plots for the anodic dissolution of NAB RDE within the filtered seawater. At each increment of angular velocity, a distinct Tafel slope was measured with increasing values of anodic current density. This behaviour is typical of that of copper [13, 17, 33]. The effect has been attributed to an irreversibility of the anodic equilibrium reaction, which can be de-polarised via the removal of $\mathrm{CuCl_2^-}$ from the Nernst diffusion layer [15], i.e., the equilibrium potential of the anodic reaction is made more negative at larger values of fluid velocity. In these cases, currents measured at the same applied potential are larger at higher fluid velocities as the total potential difference between the Reynolds number dependent equilibrium potential of the anodic reaction and the applied positive overpotential is effectively increased.

Table 2 gives a comparison of the diagnostic parameters, which have been used to characterise the apparent Tafel response of copper as a function of electrode angular velocity. These parameters are the apparent Tafel slope and the dependencies of current density on both velocity and applied potential. The experimental responses of NAB and unalloyed copper (the latter produced under identical conditions to this work [13]) correlate extremely well. Overall mean values of apparent Tafel slope for the copper and NAB electrodes were approximately 0.061 ± 0.010 and 0.058 ± 0.010 V decade^{-1}, respectively.

In this potential region, the dependency of the logarithmic current density (j) in this potential region on logarithmic angular velocity, shown in Equation 3, was also very similar between the materials with mean n values of 0.41 ± 0.03 (Cu RDE) and 0.44 ± 0.03 (NAB RDE),

$$\log(j) = k\ \log(\omega)^n \tag{3}$$

These values are close to that of 0.50 expected for full mass transfer control of the reaction rate. Because of the increased dependency of the mass transfer controlled component of RCE current density [12], the equivalent cylinder electrode values of n were larger at $=0.67 \pm 0.05$ (Cu) and 0.62 ± 0.03 (NAB). A value close to 0.70 would be expected for full mass transfer control at a hydrodynamically smooth RCE [34].

Anodic Koutecky–Levich plots (Figure 5) were used to determine pure charge transfer controlled anodic current [12]. All three sets of plots are typical of a copper-based, electrodissolution reaction, which is predominantly under diffusion control [10]. Under these circumstances, the gradient of the Koutecky–Levich slope decreases at more positive polarisation. True anodic Tafel plots (β_{A}) were derived from the y axis intercepts of the Koutecky–Levich plots at each applied potential (Figure 6). Taking α_{A} to equal the anodic charge transfer coefficient:

$$\beta_A = \frac{\alpha_A zF}{2.3RT} \tag{4}$$

Table 2. Diagnostic parameters used to characterise the experimental anodic behaviour of pure copper in chloride media applied to the experimental results of NAB

System identity	$\left(\frac{\mathrm{d}E}{\mathrm{d}\log j}\right)$ /V decade^{-1}	$\left(\frac{\mathrm{d}\log j}{\mathrm{d}\log \omega}\right)$ (log[A cm^{-2}] /log[rad s^{-1}])	$\left[\mathrm{d}E/\mathrm{d}\log\left(\frac{\mathrm{d}j}{\mathrm{d}\omega^n}\right)\right]$ (1/⌈log[A cm^{-2} / {rad s^{-1}}$^{\mathrm{n}}$]/V⌋)
Cu RDE	0.062 → 0.064	0.45 → 0.40	0.070 ± 0.002
Filtered	(0.062 ± 0.001)	(0.43 ± 0.03)	
Cu RDE	0.062 → 0.071	0.45 → 0.40	0.067 ± 0.003
Artificial	(0.066 ± 0.003)	(0.38 ± 0.04)	
Cu RCE	0.051 → 0.058	0.62 → 0.77	0.060 ± 0.002
Filtered	(0.056 ± 0.002)	(0.67 ± 0.05)	
NAB RDE	0.055 → 0.063	0.45 → 0.42	0.065 ± 0.001
Filtered	(0.059 ± 0.003)	(0.43 ± 0.02)	
NAB RDE	0.056 → 0.064	0.47 → 0.42	0.067 ± 0.002
Artificial	(0.060 ± 0.003)	(0.44 ± 0.02)	
NAB RCE	0.063 → 0.069	0.57 → 0.64	0.063 ± 0.001
Filtered	(0.065 ± 0.003)	(0.62 ± 0.03)	

Results in parenthesis indicate mean values.

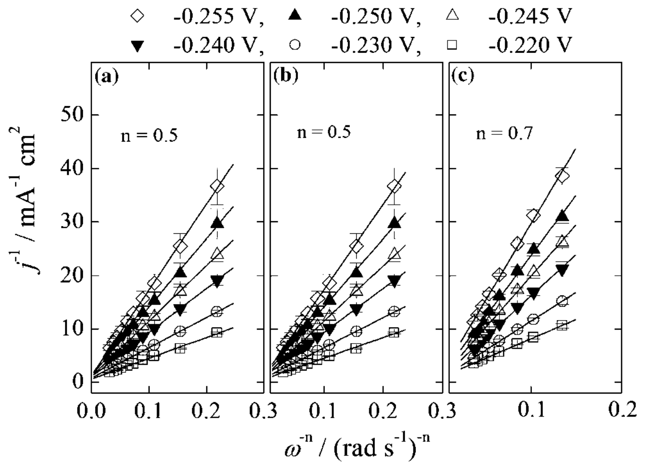

Fig. 5. Sample Koutecky–Levich plots describing RDE and RCE NAB electrodissolution within the apparent Tafel region. (a) RDE – artificial seawater, (b) RDE – filtered seawater and (c) RCE – filtered seawater.

Figure 6 describes the rate of isolated anodic charge transfer controlled current. For this data, any influence of mass transfer on the reaction rate has been removed. It is clear that there is little variation for NAB immersed in either electrolyte. For the RDE both slopes were within approximately 10 mV decade^{-1} at 0.083 ± 0.005 and 0.094 ± 0.008 V decade^{-1} for the artificial and filtered seawaters, respectively. The equivalent Tafel slope measured at the RCE was 0.091 ± 0.010 V decade^{-1}.

The 30–50% larger values of pure charge transfer controlled anodic slopes relative to the equivalent apparent Tafel slopes is the result of the removal of the mass transfer component via extrapolation to an infinite rate of mass transfer. Wood et al. [10] examined the pure charge transfer controlled anodic dissolution of copper, where the anodic Tafel slope tended towards 0.120 V decade^{-1} as the influence of mass transfer on the current was removed.

The anodic currents derived for the RCE were consistently larger than those for the RDE. This could be attributable to different grain morphology at the active electrode surfaces (observed via light microscopy). The RDE and RCE formed transverse section and longitudinal sections of the same wrought material sample. Longitudinal grains and inter-metallic phases at the RCE would dominate the extruded material and may influence the relative number of active sites and the coverage and effectiveness of a protective corrosion product film.

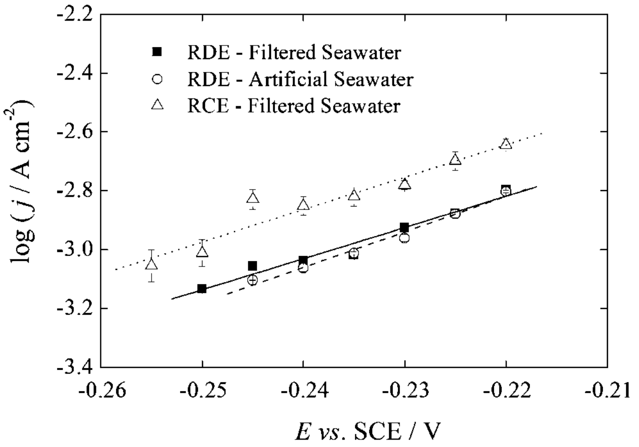

Fig. 6. Comparison of Koutecky–Levich equation derived, Tafel slopes for the anodic dissolution of the NAB RDE and RCE.

By analogy with copper [18, 23, 25, 29, 31, 32, 35] and assuming the oxidation,

$$\mathrm{Cu} + 2\mathrm{Cl}^- \rightarrow \mathrm{CuCl}_2^- + \mathrm{e}^- \tag{5}$$

which has a rate constant,

$$k_A = \frac{j}{zF[\mathrm{Cl}^-]^2} \tag{6}$$

potential dependent rate constants (k_A) were calculated at each applied potential from the experimental constants given in Table 3 (relating to Equation 7).

$$k_A = k_o \exp^{\frac{\alpha zF}{RT}(E-E_e)} = k_o \exp^{B(E-E_e)} \tag{7}$$

Here, α and k_o are the charge transfer coefficient, the electrochemical rate constant for the anodic reaction and the equilibrium potential (E_e) was assumed to be equal to −0.405 V vs SCE for this system [15]. Values of k_A were then extrapolated to the Reynolds number dependent corrosion potential. The resulting rate constants (Figure 7) give the rate of the charge transfer controlled anodic dissolution of NAB at each corrosion potential. The results again indicate that the dissolution rate of NAB is dependent on electrode geometry with the greatest rates measured at the RCE. Maximum values of k_A were produced at 21 rad s^{-1} ($Re_{\mathrm{RCE}} = 3800$; $Re_{\mathrm{RDE}} = 79$) in each case at 1.2×10^{-8} cm s^{-1} for the RCE and 3×10^{-9} cm s^{-1} for the RDE. The relatively

Table 3. Experimental constants relating to Equation 7 which describe the exponential change in the potential dependent rate constant for the anodic dissolution of NAB as a function of applied potential

Source	E vs SCE /V	E–E° /V	K$_o$ /cm s^{-1}	B
RDE – filtered seawater	−0.250 to −0.220	+0.155 to +0.185	7.0×10^{-10}	24.32
RDE – artificial seawater	−0.245 to −0.220	+0.160 to +0.185	4.0×10^{-10}	24.36
RCE – filtered seawater	−0.255 to −0.220	+0.150 to +0.185	8.0×10^{-10}	25.26

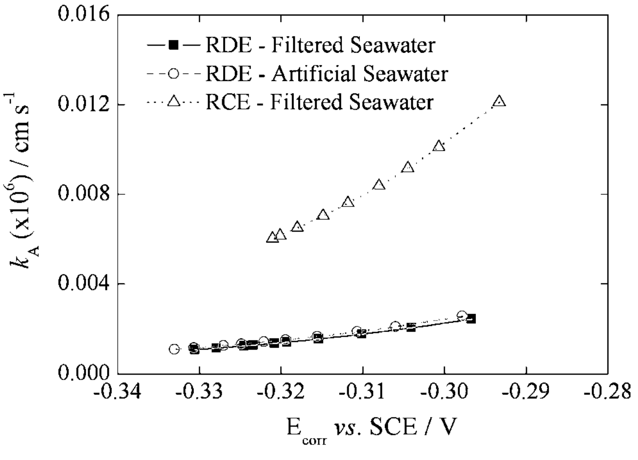

Fig. 7. Extrapolated values of potential dependent rate constant for the electrodissolution of NAB at each directly measured value of corrosion potential.

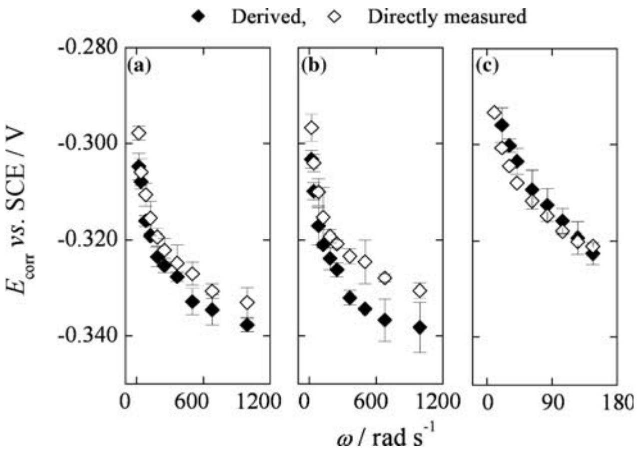

Fig. 9. Comparison of Tafel extrapolation derived and directly measured corrosion potentials. (a) RDE – artificial seawater, (b) RDE – filtered seawater and (c) RCE – filtered seawater.

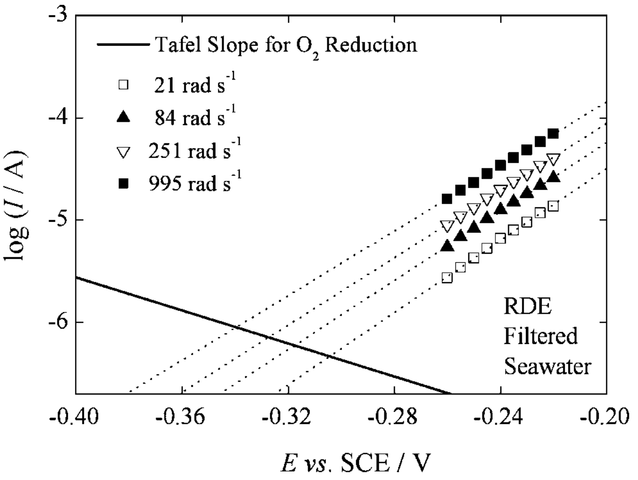

Fig. 8. Example derivation of the NAB mixed potential via Tafel slope extrapolation.

low values of k_A in all cases gives a direct indication of how important the chloride ion is for rapid alloy dissolution (see Equation 6).

3.3. *Derivation of the mixed potential*

Figure 8 is an Evans Diagram illustrating the derivation of the NAB mixed potential using extrapolated cathodic charge transfer current for O_2 reduction and the apparent Tafel slopes for mixed charge and mass transfer controlled electro dissolution. All cathodic polarisation directly measured corrosion potential data were taken from Part I [12]. In Figure 9, comparison has been made between the derived corrosion potential values taken from this approach and the directly measured corrosion potential distribution as a function of angular velocity.

From both Figures 8 and 9, it is clear that the corrosion potential of freshly polished NAB shows a significant dependence on the conditions of mass transfer. In each case the corrosion potential will become more negative in a non-linear manner as fluid velocity is ramped. The correlation between the directly measured and derived potentials is good with a maximum deviation between the mean of < 10 mV. The dependence of both the directly measured and derived corrosion potential on angular velocity can be described by the simple power law given in Equation 8.

$$E_{\text{corr}} = k_{E\text{corr}}\,\omega^x \tag{8}$$

Diagnostic plots of logarithmic E_{corr} (V vs SCE) vs logarithmic ω (rad s^{-1}) were linear in each case and were used to produce the constants relating to Equation 8. Values of the experimental constants are given in

Table 4. Experimental constants describing the dependence of NAB corrosion potential on electrode angular velocity (rad s^{-1})

Source	Measurement technique	X	$k_{E\text{corr}}$vs SCE /V	Correlation coefficient
RDE – filtered seawater	Derived	0.029 ± 0.001	−0.278 ± 0.002	0.99645
	Directly measured	0.028 ± 0.001	−0.275 ± 0.003	0.99203
RDE – artificial seawater	Derived	0.028 ± 0.001	−0.279 ± 0.001	0.99655
	Directly measured	0.029 ± 0.001	−0.274 ± 0.001	0.99719
RCE – filtered seawater	Derived	0.044 ± 0.015	−0.258 ± 0.003	0.99666
	Directly measured	0.035 ± 0.001	−0.270 ± 0.001	0.99897

Correlation coefficients refer to the diagnostic linear regression data obtained from plots of logarithmic E_{corr} vs logarithmic ω.

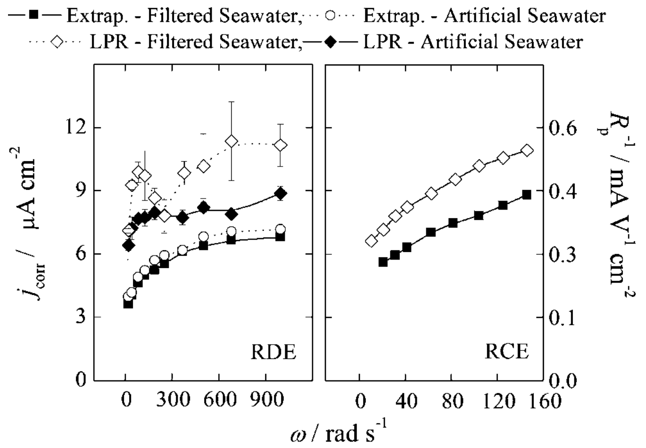

Fig. 10. Comparison of Tafel extrapolated (Extrap.) and LPR derived corrosion rates for NAB at 25 ± 0.2 °C.

Table 4. Differences in k_{Ecorr} between seawaters for the RDE were small ($\bar{k}_{E\mathrm{corr}} = -0.278 \pm 0.002$ V vs SCE). The mean estimations of the power x of 0.029 ± 0.001 (RDE) and 0.040 ± 0.006 (RCE) indicated a higher dependency of mass transfer coefficient on RCE angular velocity relative to the RDE.

The corrosion current density (j_{corr}) of NAB was largely independent of geometry and seawater type. Figure 10 gives both the Tafel extrapolated and LPR derived corrosion rates as a function of angular velocity. The Stern–Geary relationship [36] was used to independently produce instantaneous corrosion rates via polarisation resistance (R_{p}) – the slope of the E vs j curve ± 5 mV of the fully stabilised corrosion potential.

Excluding the RDE LPR data, which showed a relatively small velocity dependency, j_{corr} could also be described using a simple power law relationship:

$$j_{\mathrm{corr}} = k_{\mathrm{corr}}\omega^{x} \tag{9}$$

The constants required for the prediction of j_{corr} (mA cm^{-2}) as a function of ω (rad s^{-1}) are given in Table 5. The predicted corrosion rates for Tafel extrapolation and RCE LPR show a definite flow rate dependency and range from approximately 4 to 12 μA cm^{-2}. The low deviation of k_{corr} (0.0025 ± 0.0005 mA cm^{-2}) for both geometries and the low deviation of x values (RDE: 0.170 ± 0.003; RCE: 0.245 ± 0.018) within each geometry, describe a general similarity of NAB corrosion rate at low values of angular velocity. The LPR derived data, although less reproducible with slightly larger current densities, compare well with the corrosion rates produced via the Tafel extrapolation procedure. The maximum deviation from the mean for both techniques was around 5 μA cm^{-2}. From analogous work dealing with freshly polished copper–nickel alloys [15] it appears that elemental composition has relatively little influence over the corrosion rate of the base copper material. As can been seen in this work, however, alloying elements such as aluminium can bring character to the materials on the formation of surface films.

The previously unexamined corrosion mechanism of polished NAB in seawater has been elucidated, where it is clear that the behaviour of the freshly polished alloy is analogous to that of pure copper. Good correlation between experimental data has been demonstrated via a number of electrochemical techniques. At the corrosion potential charge transfer controlled oxygen reduction at the polished NAB dominates the cathodic half-cell. The chloride ion facilitated selective dissolution of the copper forms the anodic component, which is under a form of mixed mass and charge transfer control.

Conclusions

1. A potential step, current transient technique has been used at low values of positive polarisation to accurately determine the flow dependency of NAB dissolution under conditions of controlled laminar and turbulent fluid flow.
2. At potentials close to E_{corr}, the short-term anodic polarisation behaviour of freshly polished BS CA 104 NAB in dilute chloride media is analogous to unalloyed copper where the reaction rate is controlled by a combination of both charge and mass transfer.
3. At the corrosion potential, the charge transfer controlled reduction of oxygen and the mixed charge and mass transfer controlled electrodissolution determine the corrosion behaviour of the freshly polished material.

Table 5. Experimental constants describing the dependence of NAB corrosion rate (mA cm^{-2}) on electrode angular velocity (rad s^{-1})

Source	Technique	x	k_{corr} /mA cm^{-2}	Correlation coefficient
RDE – filtered	Extrap.	0.172 ± 0.005	0.002 ± 0.001	0.99632
RDE – artificial	Extrap.	0.168 ± 0.007	0.002 ± 0.001	0.99357
RCE – filtered	Extrap.	0.232 ± 0.010	0.003 ± 0.001	0.99470
RDE – filtered	LPR	–	–	–
RDE – artificial	LPR	–	–	–
RCE – artificial	LPR	0.257 ± 0.010	0.003 ± 0.001	0.99575

Correlation coefficients refer to the diagnostic linear regression data obtained from plots of logarithmic j_{corr} vs logarithmic ω.

4. Corrosion rates derived from Tafel extrapolation were proportional to both electrode angular velocity and geometry and ranged from approximately 4 to 12 μA cm^{-2} in filtered and artificial seawaters at 25 ± 0.2 °C.
5. LSV has been used to examine the passivation characteristics of NAB as a function of fluid velocity. At relatively high RDE angular velocities (>188 rad s^{-1}, 1800 rpm), the material exhibited a self-passivating mechanism which significantly improved to dissolution resistance.
6. The Al_2O_3-based passivation mechanism of the material was found to be dependent on both applied potential and ambient mass transfer conditions.

Acknowledgements

The authors are grateful to DSTL-Farnborough, UK and QinetQ-Haslar, UK for financial contributions to the research programme.

References

1. R.W. Cahn, P. Hassen and E.J. Kramer, Materials science and technology, a comprehensive treatment, *in* '*Structure and Properties of Nonferrous Alloys*', Vol. 8 (VCH, New York, 1996).
2. A. Schussler and H.E. Exner, *Corros. Sci.* **34** (1993) 1793.
3. A. Schussler and H.E. Exner, *Corros. Sci.* **34** (1993) 1803.
4. E.A. Culpan and G. Rose, *Brit. Corros. J.* **14** (1979) 160.
5. A. Al-Hashem, P.G. Caceres, W.T. Riad and H.M. Shalaby, *Corrosion* **51** (1995) 331.
6. L. Kenworthy, *Trans. Inst. Marine Eng.* **77** (1965) 149.
7. J.R. Scully, H.P. Hack and D.G. Tipton, *Corrosion* **42** (1986) 462.
8. R. Francis, *Brit. Corros. J.* **34** (1999) 139.
9. A Working Party Report, European Federation of Corrosion Publications No. 5, 'Illustrated Case Histories of Marine Corrosion', Technical Report (The Institute of Metals, London, 1990).
10. R.J.K. Wood, S.P. Hutton and D.J. Schiffrin, *Corros. Sci.* **30** (1990) 1177.
11. K.D. Efird, *Corrosion-NACE* **33** (1977) 3.
12. G. Kear, F.C. Walsh, B.D. Barker and K. Stokes, *J. Appl. Electrochem.*, submitted for publication.
13. G. Kear, F.C. Walsh, D.B. Barker and K.S. Stokes, Electrochemical Corrosion Characteristics of Copper in Filtered and Artificial Seawater as a Function of Mass Transfer Conditions, *in* 'Proceedings of EuroCorr 2000, Queen Mary and Westfield College', University of London, Institute of Corrosion, 10–14 September 2000.
14. G. Kar, T.W. Healy and D.W. Fuerstenau, *Corros. Sci.* **13** (1973) 375.
15. G. Kear, Electrochemical corrosion of marine alloys under flowing conditions, Dissertation, University of Portsmouth, Hampshire, UK (2001).
16. G.P. Power and I.M. Ritchie, *Electrochim. Acta* **26** (1981) 1073.
17. G. Kear, D.B. Barker and F.C. Walsh, *Corros. Sci.* **46** (2004) 109.
18. H.P. Lee and K. Nobe, *J. Electrochem. Soc.* **133** (1986) 2035.
19. M. Braun and K. Nobe, *J. Electrochem. Soc.* **126** (1979) 1666.
20. G. Faita, G. Fiori and D. Salvadore, *Corr. Sci.* **15** (1975) 383.
21. J.C. Scully, 'The Fundamentals of Corrosion' (Pergamon Press, Oxford, 1990).
22. B.D. Craig, 'Fundamental Aspects of Corrosion Films in Corrosion Science' (Plenum Press, London, 1991).
23. A.L. Bacarella and J.C. Griess, *J. Electrochem. Soc.* **120** (1973) 459.
24. P.A. Lush and M.J. Carr, *Corros. Sci.* **19** (1979) 1079.
25. A. Moreau, *Electrochim. Acta* **26** (1981) 497.
26. S.R. de Sanchez and D.J. Schiffrin, *Corros. Sci.* **22** (1982) 585.
27. S.R. de Sanchez and D.J. Schiffrin, *Corros. Sci.* **28** (1988) 141.
28. L. Brossard, *J. Electrochem. Soc.* **130** (1983) 403.
29. B. Tribollet and J. Newman, *J. Electrochem. Soc.* **131** (1984) 2780.
30. H.P. Dhar, R.E. White, G. Burnell, L.R. Cornwell, R.B. Griffin and R. Darby, *Corrosion* **41** (1985) 317.
31. W.H. Smyrl, *J. Electrochem. Soc.* **132** (1985) 1556.
32. C. Deslouis, B. Tribollet, G. Mengoli and M. Musiani, *J. Appl. Electrochem.* **18** (1988) 374.
33. H. Lal and H.R. Thirsk, *J. Chem. Soc.* **100** (1953) 2638.
34. M. Eisenberg, C.W. Tobias and C.R. Wilke, *Chem. Eng. Prog. Symp. Ser.* **51** (1954) 1.
35. F. King, C.D. Litke, M.J. Quin and D.M. LeNeveu, *Corros. Sci.* **37** (1995) 833.
36. M. Stern and A.L. Geary, *J. Electrochem. Soc.* **104** (1957) 56.